Vibrational Stability Effects in Rotorcraft Flight Dynamics

Umberto Saetti
Assistant Professor
Department of Aerospace Engineering
University of Maryland
College Park, MD 20740

Zhouzhou Chen
Graduate Research Assistant
Joseph F. Horn
Professor
Department of Aerospace Engineering
Pennsylvania State University
University Park, PA 16802

Tom Berger
Flight Controls Group Lead
U.S. Army Combat Capabilities Development
Command Aviation & Missile
Moffett Field, CA 94035

ABSTRACT

This paper investigates vibrational stabilization effects in rotorcraft flight dynamics. This study is motivated by the fact that eigenvalues of the rotorcraft flight dynamics identified from flight test often differ from those computed with physics-based simulations, and that some commonly observed mismatches may be ascribed to vibrational stability effects due to rotor blade imbalance or other periodic disturbance on the rotorcraft. Starting from a simple example involving an inverted pendulum, the paper demonstrates the use of the harmonic decomposition method for the study of vibrational stabilization effects. The concept is then extended to analyze the effect of blade imbalance on the flight dynamics of a helicopter. Additionally, vibrational stablization of a slung load in forward flight is investigated using small-amplitude and disturbances on an active cargo hook. Results show that while vibrations induced by rotor blade imbalance do not stabilize the hovering dynamics of a helicopter, these vibrations still have a significant effect on the hovering dynamics. Rotor blade imbalance results in a symmetric effect on the roll and pitch axes, in that it tends to decrease the frequency of the subsidence modes of the hovering cubic, while the unstable oscillatory modes tend to increase in frequency and decrease in damping. On the other hand, the yaw/heave dynamics are relatively unaffected compared to the lateral and longitudinal axes. Moreover, small-amplitude oscillations of an active cargo hook were shown to significantly decrease the amplitude of the limit cycle oscillation of a slung load in forward flight and to stabilize its dynamics. This constitutes a practical solution to the semi-active control of a suspended load.

INTRODUCTION

Vibrational stabilization is a phenomena where the unstable dynamics of a system about an equilibrium point of interest can be stabilized via periodic forcing of the system at a high-enough forcing frequency (Refs. 1, 2). Examples of this phenomena include, but are not limited to, those involving an inverted pendulum with vibrating suspension point (Ref. 3) and hovering insects where their hovering cubic (Ref. 4) is stabilized by the wing periodic flapping motion (Ref. 5, 6). In the latter case, the wing flapping motion inducing a vibrational stabilization mechanism that increases the pitch damping and stiffness while reducing the speed stability. This results in stabilization of the pitch oscillatory mode and thus of the longitudinal hovering cubic.

Presented at the 49th European Rotorcraft Forum, Bückeburg, Germany, September 5–7, 2023.

Despite apparent differences in shape and dimension, the dynamics of flapping-wing flyers is indeed mathematically similar to those of rotary-wing vehicles such as helicopters. This stems from the time-varying aerodynamic and inertial loads due to the wing/blade periodic motion. In fact, the dynamics of both flapping- and rotary-wing flight is described by nonlinear time-periodic (NLTP) systems of the coupled rigid-body and complex interactional aerodynamics between the wings/blades, body, and the self-induced wake. However, the relative importance of the time-periodic dynamics (*i.e.*, those dynamics with natural frequencies that are multiples of the fundamental frequency of the system) and the overall dynamics of the system (*i.e.*, averaged + time-periodic dynamics) is significantly higher for flapping-wing flyers than it is for helicopters – approximately 7% for helicopters (Ref. 7) and up to 50% for flapping-wing flyers (Ref. 8, 9).

In light of these similarities, vibrational stabilization mechanisms that are observed for flapping-wing flight might also extend to rotary-wing vehicles. One indication of this comes from anecdotal evidence suggesting that eigenvalues of the rotorcraft flight dynamics identified from flight test often differ from those computed with physics-based simulations. In fact, these commonly observed mismatches may be ascribed to vibrational stability effects due to rotor blade imbalance or other periodic disturbance on the rotorcraft. Another instance of vibrational stabilization comes from from slung load carriage, where previous research has shown that slung loads can exhibit better stability /lower amplitude oscillations when subjected to periodic disturbances at the hook (Ref. 10). As such, the objective of this paper is to investigate vibrational stabilization effects on the flight dynamics of rotorcraft.

One major challenge in the analysis of vibrational stabilization lies in the stability analysis of NLTP systems. While the stability analysis of nonlinear time-invariant (NLTI) systems is readily assessed by linearizing the dynamics about an equilibrium point and performing eigenanalysis, or by means of Lyapounov theory, the stability analysis of NLTP systems is typically a more challenging task. This is because the equilibrium solution of NLTP systems is typically represented by a periodic orbit rather than by a fixed point. Two main approaches exist for determining the stability of NLTP systems (Fig. 1), as articulated in Ref. 11: the first is based on Floquet theory (Refs. 12–16) and the is second based on averaging methods (Refs. 11, 17–25). The first approach is articulated in the following four major steps: (i) a periodic orbit is found by solving the dynamic equations, (ii) the dynamic equations are linearized about that periodic orbit to yield a linear time-periodic (LTP) system, (iii) the LTP system is transformed into a linear time-invariant (LTI) system via Floquet transformation/decomposition, and (iv) stability is assessed by checking the eigenvalues of the LTI system. The second approach to determine stability of NLTP systems leverages averaging methods to transform the NLTP system into an equivalent NLTI system where the periodic orbit of the original system collapses to a single point in the state space. Stability is thus assessed by linearizing the equivalent NLTI system about its equilibrium point and by performing spectral analysis (Ref. 17).

Historically, the only methods available for transforming the LTP dynamics into approximate higher-order LTI systems were the Lyapounov-Floquet method (Ref. 26) and frequency lifting methods (Ref. 27), which both suffered from the common disadvantage of the need for state transition matrices. State transition matrices constitute a particular challenge in that their computation can be numerically intensive and/or very sensitive to tuning parameters which require prior knowledge on the system's dynamics. However, this limitation was recently relaxed by the *harmonic decomposition* method that originated from the rotorcraft community (Refs. 28–30). Within the context of rotorcraft, harmonic decomposition models have been used to: (i) study the interference effects between higher-harmonic control (HHC) and the aircraft flight control system (AFCS) (Refs. 28, 31–33); (ii) design load alleviation control (LAC) laws (the PI's efforts in Refs. 34–36); and (iii) prediction and avoidance of flight envelope limits (Refs. 36–38). A survey by the PI on the use of harmonic decomposition models in the rotorcraft field can be found in Ref. 39. When coupled with a harmonic balance scheme, harmonic decomposition can also be used to solve for (stable and unstable) periodic solutions (Ref. 40) and compute open-loop higher-harmonic control (HHC) inputs that attenuate arbitrary state/output harmonics (Ref. 9). Because harmonic decomposition (i) relaxes all limitations associated with the Floquet-based approach and (ii) can be used to compute unstable periodic orbits (note that the unaugmented hover dynamics of rotorcraft is unstable, see Ref. 4), it is used to analyze vibrational stability of rotorcraft in this study.

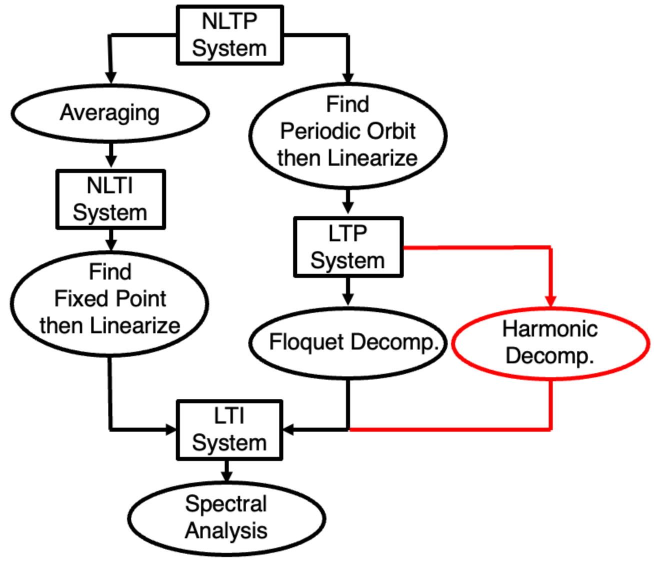

Fig. 1: Illustration of the two main approaches to stability analysis of NLTP systems: averaging methods (left), Floquet theory and harmonic decomposition (right).

The paper starts from a simple example involving an inverted pendulum to demonstrate the use of the harmonic decomposition method (Ref. 28, 29) for the study of vibrational stabilization effects. The concept is then extended to analyze the effect of blade imbalance on the flight dynamics of a helicopter, as well as vibrational stablization of a slung load in forward flight using small-amplitude and disturbances on an active cargo hook. Final remarks summarize the overall findings of the study and future developments are identified.

METHODOLOGY

Mathematical Background

Consider a nonlinear time-periodic (NLTP) system in first-order form representative of the rotorcraft flight dynamics:

$$\dot{\boldsymbol{x}} = \boldsymbol{f}(\boldsymbol{x}, \boldsymbol{u}, t) \tag{1a}$$

$$\boldsymbol{y} = \boldsymbol{g}(\boldsymbol{x}, \boldsymbol{u}, t) \tag{1b}$$

where $\boldsymbol{x} \in \mathbb{R}^n$ is the state vector, $\boldsymbol{u} \in \mathbb{R}^m$ is the control input vector, $\boldsymbol{y} \in \mathbb{R}^l$ is the output vector, and t is the dimensional time in seconds. The nonlinear functions $\boldsymbol{f}$ and $\boldsymbol{g}$ are

T-periodic in time such that:

$$\boldsymbol{f}(\boldsymbol{x},\boldsymbol{u},t)=\boldsymbol{f}(\boldsymbol{x},\boldsymbol{u},t+T) \tag{2a}$$

$$\boldsymbol{g}(\boldsymbol{x},\boldsymbol{u},t)=\boldsymbol{g}(\boldsymbol{x},\boldsymbol{u},t+T) \tag{2b}$$

Note that the fundamental period of the system is $T=\frac{2\pi}{\Omega}$ seconds, where Ω is the angular speed of the main rotor in rad/s. Let $\boldsymbol{x}^*(t)$ and $\boldsymbol{u}^*(t)$ represent a periodic solution of the system such that $\boldsymbol{x}^*(t)=\boldsymbol{x}^*(t+T)$ and $\boldsymbol{u}^*(t)=\boldsymbol{u}^*(t+T)$. Then, the NLTP system can be linearized about the periodic solution. Consider the case of small disturbances:

$$\boldsymbol{x}=\boldsymbol{x}^*+\boldsymbol{\Delta x} \tag{3a}$$

$$\boldsymbol{u}=\boldsymbol{u}^*+\boldsymbol{\Delta u} \tag{3b}$$

where $\boldsymbol{\Delta x}$ and $\boldsymbol{\Delta u}$ are the state and control perturbation vectors from the candidate periodic solution. A Taylor series expansion is performed on the state derivative and output vectors. Neglecting terms higher than first order results in the following equations:

$$\boldsymbol{f}\left(\boldsymbol{x}^*+\boldsymbol{\Delta x},\boldsymbol{u}^*+\boldsymbol{\Delta u},t\right)=\boldsymbol{f}\left(\boldsymbol{x}^*,\boldsymbol{u}^*,t\right)+\boldsymbol{F}(t)\boldsymbol{\Delta x}+\boldsymbol{G}(t)\boldsymbol{\Delta u} \tag{4a}$$

$$\boldsymbol{g}\left(\boldsymbol{x}^*+\boldsymbol{\Delta x},\boldsymbol{u}^*+\boldsymbol{\Delta u},t\right)=\boldsymbol{g}\left(\boldsymbol{x}^*,\boldsymbol{u}^*,t\right)+\boldsymbol{P}(t)\boldsymbol{\Delta x}+\boldsymbol{Q}(t)\boldsymbol{\Delta u} \tag{4b}$$

where:

$$\boldsymbol{F}(t)=\left.\frac{\partial \boldsymbol{f}(\boldsymbol{x},\boldsymbol{u})}{\partial \boldsymbol{x}}\right|_{\boldsymbol{x}^*,\boldsymbol{u}^*}, \quad \boldsymbol{G}(t)=\left.\frac{\partial \boldsymbol{f}(\boldsymbol{x},\boldsymbol{u})}{\partial \boldsymbol{u}}\right|_{\boldsymbol{x}^*,\boldsymbol{u}^*} \tag{5a-b}$$

$$\boldsymbol{P}(t)=\left.\frac{\partial \boldsymbol{g}(\boldsymbol{x},\boldsymbol{u})}{\partial \boldsymbol{x}}\right|_{\boldsymbol{x}^*,\boldsymbol{u}^*}, \quad \boldsymbol{Q}(t)=\left.\frac{\partial \boldsymbol{g}(\boldsymbol{x},\boldsymbol{u})}{\partial \boldsymbol{u}}\right|_{\boldsymbol{x}^*,\boldsymbol{u}^*} \tag{5c-d}$$

Note that the state-space matrices in Eq. (5) have T-periodic coefficients such that:

$$\boldsymbol{F}(t)=\boldsymbol{F}(t+T), \quad \boldsymbol{G}(t)=\boldsymbol{G}(t+T) \tag{6a-b}$$

$$\boldsymbol{P}(t)=\boldsymbol{P}(t+T), \quad \boldsymbol{Q}(t)=\boldsymbol{Q}(t+T) \tag{6c-d}$$

Equations (4a) and (4b) yield a linear time-periodic (LTP) approximation of the NLTP system of Eq. (1) as follows:

$$\boldsymbol{\Delta\dot{x}}=\boldsymbol{F}(t)\boldsymbol{\Delta x}+\boldsymbol{G}(t)\boldsymbol{\Delta u} \tag{7a}$$

$$\boldsymbol{\Delta y}=\boldsymbol{P}(t)\boldsymbol{\Delta x}+\boldsymbol{Q}(t)\boldsymbol{\Delta u} \tag{7b}$$

Hereafter, the notation is simplified by dropping the Δ in front of the linearized perturbation state and control vectors while keeping in mind that these vectors represent perturbations from a periodic equilibrium. Next, the state, input, and output vectors of the LTP systems are decomposed into a finite number of harmonics of the fundamental period via Fourier analysis:

$$\boldsymbol{x}=\boldsymbol{x}_0+\sum_{i=1}^{N}\boldsymbol{x}_{ic}\cos\left(\frac{2\pi it}{T}\right)+\boldsymbol{x}_{is}\sin\left(\frac{2\pi it}{T}\right) \tag{8a}$$

$$\boldsymbol{u}=\boldsymbol{u}_0+\sum_{j=1}^{M}\boldsymbol{u}_{jc}\cos\left(\frac{2\pi jt}{T}\right)+\boldsymbol{u}_{js}\sin\left(\frac{2\pi jt}{T}\right) \tag{8b}$$

$$\boldsymbol{y}=\boldsymbol{y}_0+\sum_{k=1}^{L}\boldsymbol{y}_{kc}\cos\left(\frac{2\pi kt}{T}\right)+\boldsymbol{y}_{ks}\sin\left(\frac{2\pi kt}{T}\right) \tag{8c}$$

As shown in Ref. 28, the harmonic decomposition methodology can be used to transform the LTP model into an approximate higher-order linear time-invariant (LTI) model in first-order form:

$$\dot{\boldsymbol{X}}=\boldsymbol{A}\boldsymbol{X}+\boldsymbol{B}\boldsymbol{U} \tag{9a}$$

$$\boldsymbol{Y}=\boldsymbol{C}\boldsymbol{X}+\boldsymbol{D}\boldsymbol{U} \tag{9b}$$

where the augmented state, control, and output vectors $\boldsymbol{X}\in\mathbb{R}^{n(2N+1)}$, $\boldsymbol{U}\in\mathbb{R}^{m(2M+1)}$, and $\boldsymbol{Y}\in\mathbb{R}^{l(2L+1)}$, respectively, are given by:

$$\boldsymbol{X}^T=\left[\boldsymbol{x}_0^T\ \boldsymbol{x}_{1c}^T\ \boldsymbol{x}_{1s}^T\ \ldots\ \boldsymbol{x}_{Nc}^T\ \boldsymbol{x}_{Ns}^T\right] \tag{10a}$$

$$\boldsymbol{U}^T=\left[\boldsymbol{u}_0^T\ \boldsymbol{u}_{1c}^T\ \boldsymbol{u}_{1s}^T\ \ldots\ \boldsymbol{u}_{Mc}^T\ \boldsymbol{u}_{Ms}^T\right] \tag{10b}$$

$$\boldsymbol{Y}^T=\left[\boldsymbol{y}_0^T\ \boldsymbol{y}_{1c}^T\ \boldsymbol{y}_{1s}^T\ \ldots\ \boldsymbol{y}_{Lc}^T\ \boldsymbol{y}_{Ls}^T\right] \tag{10c}$$

with $\boldsymbol{A}\in\mathbb{R}^{n(2N+1)\times n(2N+1)}$, $\boldsymbol{B}\in\mathbb{R}^{n(2N+1)\times m(2M+1)}$, $\boldsymbol{C}\in\mathbb{R}^{l(2L+1)\times n(2N+1)}$, and $\boldsymbol{D}\in\mathbb{R}^{l(2L+1)\times m(2M+1)}$. Closed-form expressions for these matrices can be found in Ref. 28. It is worth noting that harmonic decomposition does not rely on state transition matrices, which makes the methodology more computationally efficient and less numerically sensitive than other approaches such as the Lyapounov-Floquet method (Ref. 26) and frequency lifting methods (Ref. 27).

Model-Order Reduction

Because one of the objective of this paper is to investigate the change in stability derivatives that results from vibrational stabilization, it is desired to reduce the order of the harmonic decomposition models down to a model that is representative of rigid-body dynamics. Ideally, these reduced-order models do not include the higher harmonic states but still retain part of the higher-harmonic response characteristics. This can be achieved through residualization, a portion of singular perturbation theory that pertains to LTI systems (Ref. 41). Assuming that one or more states of the system have stable dynamics which are faster than that of the remaining states, the state vector in Eq. (10a) can be partitioned into fast $\boldsymbol{X}_\text{f}$ and slow $\boldsymbol{X}_\text{s}$ components:

$$\boldsymbol{X}^T=\left[\boldsymbol{X}_\text{s}^T\ \boldsymbol{X}_\text{f}^T\right] \tag{11}$$

Then, the system in Eq. (9a) can be re-written as:

$$\begin{bmatrix}\dot{\boldsymbol{X}}_\text{s}\\ \dot{\boldsymbol{X}}_\text{f}\end{bmatrix}=\begin{bmatrix}\boldsymbol{A}_\text{s} & \boldsymbol{A}_\text{sf}\\ \boldsymbol{A}_\text{fs} & \boldsymbol{A}_\text{f}\end{bmatrix}\begin{bmatrix}\boldsymbol{X}_\text{s}\\ \boldsymbol{X}_\text{f}\end{bmatrix}+\begin{bmatrix}\boldsymbol{B}_\text{s}\\ \boldsymbol{B}_\text{f}\end{bmatrix}\boldsymbol{U} \tag{12}$$

By neglecting the dynamics of the fast states (*i.e.*, $\dot{\boldsymbol{X}}_\text{f}=0$) and performing a few algebraic manipulations, the equations for a reduced-order system with the state vector composed of the slow states may be found:

$$\dot{\boldsymbol{X}}_\text{s}=\hat{\boldsymbol{A}}\boldsymbol{X}_\text{s}+\hat{\boldsymbol{B}}\boldsymbol{U} \tag{13}$$

where:

$$\hat{\boldsymbol{A}}=\boldsymbol{A}_\text{s}-\boldsymbol{A}_\text{sf}\boldsymbol{A}_\text{f}^{-1}\boldsymbol{A}_\text{fs} \tag{14a}$$

$$\hat{\boldsymbol{B}}=\boldsymbol{B}_\text{s}-\boldsymbol{A}_\text{sf}\boldsymbol{A}_\text{f}^{-1}\boldsymbol{B}_\text{f} \tag{14b}$$

Note that $\boldsymbol{A}_\text{f}$ must be invertible. This is guaranteed if $\boldsymbol{A}_\text{f}$ is non-singular, *i.e.*, no eigenvalue has a real-part that is equal to zero. Additionally, to apply residualization, $\boldsymbol{A}_\text{f}$ must be is asymptotically stable, *i.e.*, all eigenvalues have their real part that is strictly negative. In this study, the slow states are chosen as the zeroth harmonic rigid-body states with the exception of the position states as the flight dynamics are invariant with respect to these (42), whereas the fast states are taken as the higher harmonics of the rotor states:

$$\boldsymbol{X}_\text{s}^T = \left[u_0\ v_0\ w_0\ p_0\ q_0\ r_0\ \phi_0\ \theta_0\ \psi_0\right] \tag{15a}$$

$$\boldsymbol{X}_\text{f}^T = \left[\boldsymbol{x}_{\text{R}_0}^T\ \boldsymbol{x}_{\text{R}_{1c}}^T\ \cdots\ \boldsymbol{x}_{\text{R}_{Ns}}^T\right] \tag{15b}$$

where $\boldsymbol{x}_\text{R}$ are the rotor states. The rotor states are generally asymptotically stable, unless there is some aeromechanic/aeroelastic instability, which is not modelled herein anyway. This guarantees $\boldsymbol{A}_\text{f}$ to be asymptotically stable. Note that the higher harmonics of the rigid-body states were truncated from the fast state vector. This is because the higher harmonics of the rigid-body states are generally unstable at hover and low-to-moderate speeds (their eigenvalues are shifted on the imaginary axis with respect to the zeroth-harmonic eigenvalues by $k\Omega$, with $k = 1,\ldots,N$). This would cause $\boldsymbol{A}_\text{f}$ not to be asymptotically stable. The truncation of these states is justified by the fact that the higher harmonics of the rigid body states have negligible contribution to the overall flight dynamics (Ref. 7). An alternative reduction that yields a 10-state model involves retaining the longitudinal and lateral flapping angles as part of the slow state vector, such that:

$$\boldsymbol{X}_\text{s}^T = \left[u_0\ v_0\ w_0\ p_0\ q_0\ r_0\ \phi_0\ \theta_0\ \psi_0\ \beta_{1c}\ \beta_{1s}\right] \tag{16a}$$

$$\boldsymbol{X}_\text{f}^T = \left[\hat{\boldsymbol{x}}_{\text{R}_0}^T\ \boldsymbol{x}_{\text{R}_{1c}}^T\ \cdots\ \boldsymbol{x}_{\text{R}_{Ns}}^T\right] \tag{16b}$$

where $\hat{\boldsymbol{x}}_{\text{R}_0}$ is the zeroth harmonic of the rotor state vector with the longitudonal and lateral flapping states removed. The 10-state model will model the regressive flap mode and be accurate, at least for the UH-60 helicopter, up to about 10 rad/s, compared to approximately the 4 rad/s of the 8-state model retaining the rigid-body dynamics only (Refs. 43, 44). Both methods are used in this paper.

To ensure the residualized model retains information about the influence of the residualized dynamics on both the zeroth harmonics and the higher output harmonics of the output, consider partitioning the output equations in Eq. (9b) as:

$$\boldsymbol{Y} = \begin{bmatrix}\boldsymbol{C}_\text{s} & \boldsymbol{C}_\text{f}\end{bmatrix}\begin{bmatrix}\boldsymbol{X}_\text{s}\\ \boldsymbol{X}_\text{f}\end{bmatrix} + \boldsymbol{DU} \tag{17}$$

Then, it can be shown that the residualized output equations are:

$$\dot{\boldsymbol{Y}} = \hat{\boldsymbol{C}}\boldsymbol{X}_\text{s} + \hat{\boldsymbol{D}}\boldsymbol{U} \tag{18}$$

where:

$$\hat{\boldsymbol{C}} = \boldsymbol{C}_\text{s} - \boldsymbol{C}_\text{f}\boldsymbol{A}_\text{f}^{-1}\boldsymbol{A}_\text{fs} \tag{19a}$$

$$\hat{\boldsymbol{D}} = \boldsymbol{D} - \boldsymbol{C}_\text{f}\boldsymbol{A}_\text{f}^{-1}\boldsymbol{B}_\text{f} \tag{19b}$$

If now the augmented output vector is selected to coincide with the harmonics of the output vector in Eq. (20), such that:

$$\boldsymbol{Y}^T = \left[\boldsymbol{y}_0^T\ \boldsymbol{y}_{1c}^T\ \boldsymbol{y}_{1s}^T\ \ldots\ \boldsymbol{y}_{Lc}^T\ \boldsymbol{y}_{Ls}^T\right] \tag{20}$$

then, the residualized model will predict the influence of the residualized dynamics on the zeroth and higher-harmonic of the output.

Vibrational Stabilization

The overall methodology used for this investigation is explained through a simple example involving an inverted pendulum (Ref. 3, 45) with a vibrating suspension point, shown in Fig. 2. Consider the dynamics of such pendulum:

$$L\ddot{\theta} - (g + A)\theta = 0 \tag{21}$$

where L is the pendulum length, A the acceleration resulting from the periodic displacement of the point of suspension, and g is the gravitational acceleration.

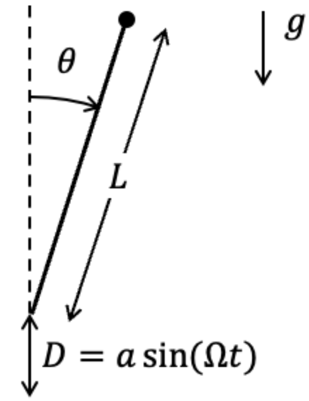

Fig. 2: Inverted pendulum with the point of suspension being vibrated.

Assume that the displacement of the point of suspension is given by:

$$D = a\sin\psi \tag{22}$$

where $\psi = \Omega t$. Then, the acceleration A of the suspension point is:

$$A = \ddot{D} = -a\Omega^2\sin\psi \tag{23}$$

The system in Eq. (21) can be reformulated as a system of ordinary differential equations (ODEs) such that:

$$\dot{\boldsymbol{x}} = \begin{bmatrix}0 & \frac{g}{L} - \frac{a}{L}\Omega^2\sin\psi\\ 0 & 1\end{bmatrix}\boldsymbol{x} = \boldsymbol{F}(\psi)\boldsymbol{x} \tag{24}$$

where $\boldsymbol{x}^T = \begin{bmatrix}\dot{\theta} & \theta\end{bmatrix}$. Note that $\boldsymbol{F}(\psi) = \boldsymbol{F}(\psi + \Omega T)$, where $T = 2\pi/\Omega$. Thus, the system in Eq. (24) is a linear time-periodic (LTP) system.

Consider now decomposing the state vector into harmonics of the fundamental frequency Ω, such that:

$$\boldsymbol{x} = \boldsymbol{x}_0 + \sum_{n=1}^{N}\left[\boldsymbol{x}_{nc}\cos(n\psi) + \boldsymbol{x}_{ns}\sin(n\psi)\right] \tag{25}$$

Then, it can be shown (Ref. 28, 29) that the system in Eq. (24) is approximated with a higher-order linear time-invariant (LTI) system of the form:

$$\dot{\boldsymbol{X}} = \boldsymbol{AX} \tag{26}$$

where $\boldsymbol{X}^T = \left[\boldsymbol{x}_0^T\ \boldsymbol{x}_{1c}^T\ \boldsymbol{x}_{1s}^T\ \dots\ \boldsymbol{x}_{Nc}^T\ \boldsymbol{x}_{Ns}^T\right]$ is the augmented state vector and:

$$\boldsymbol{A} = \left[\begin{array}{cccccc} \boldsymbol{H}_{0\boldsymbol{F}} & \boldsymbol{H}_{0\boldsymbol{F}^{1c}} & \boldsymbol{H}_{0\boldsymbol{F}^{1s}} & \cdots & \boldsymbol{H}_{0\boldsymbol{F}^{Nc}} & \boldsymbol{H}_{0\boldsymbol{F}^{Ns}} \\ \boldsymbol{H}_{1c\boldsymbol{F}} & \boldsymbol{H}_{1c\boldsymbol{F}^{1s}} & -\Omega+\boldsymbol{H}_{1c\boldsymbol{F}^{1s}} & \cdots & \boldsymbol{H}_{1c\boldsymbol{F}^{Nc}} & \boldsymbol{H}_{1c\boldsymbol{F}^{Ns}} \\ \boldsymbol{H}_{1s\boldsymbol{F}} & \Omega+\boldsymbol{H}_{1s\boldsymbol{F}^{1s}} & \boldsymbol{H}_{1s\boldsymbol{F}^{1s}} & \cdots & \boldsymbol{H}_{1s\boldsymbol{F}^{Nc}} & \boldsymbol{H}_{1s\boldsymbol{F}^{Ns}} \\ \vdots & \vdots & \vdots & \ddots & \vdots & \vdots \\ \boldsymbol{H}_{Nc\boldsymbol{F}} & \boldsymbol{H}_{Nc\boldsymbol{F}^{1s}} & \boldsymbol{H}_{Nc\boldsymbol{F}^{1s}} & \cdots & \boldsymbol{H}_{Nc\boldsymbol{F}^{Nc}} & -N\Omega+\boldsymbol{H}_{Nc\boldsymbol{F}^{Ns}} \\ \boldsymbol{H}_{Ns\boldsymbol{F}} & \boldsymbol{H}_{Ns\boldsymbol{F}^{1s}} & \boldsymbol{H}_{Ns\boldsymbol{F}^{1s}} & \cdots & N\Omega+\boldsymbol{H}_{Ns\boldsymbol{F}^{Nc}} & \boldsymbol{H}_{Ns\boldsymbol{F}^{Ns}} \end{array}\right] \tag{27}$$

The $\boldsymbol{A}$ matrix coefficients are given by:

$$\boldsymbol{H}_{0\boldsymbol{M}} = \frac{1}{2\pi}\int_0^{2\pi} \boldsymbol{F}(\psi)d\psi \tag{28a}$$
$$\boldsymbol{H}_{ic\boldsymbol{M}} = \frac{1}{\pi}\int_0^{2\pi} \boldsymbol{F}(\psi)\cos(n\psi)d\psi \tag{28b}$$
$$\boldsymbol{H}_{is\boldsymbol{M}} = \frac{1}{\pi}\int_0^{2\pi} \boldsymbol{F}(\psi)\sin(n\psi)d\psi \tag{28ba-c}$$
$$\boldsymbol{H}_{0\boldsymbol{F}^{nc}} = \frac{1}{2\pi}\int_0^{2\pi} \boldsymbol{F}^{nc}(\psi)d\psi \tag{28c}$$
$$\boldsymbol{H}_{ic\boldsymbol{F}^{nc}} = \frac{1}{\pi}\int_0^{2\pi} \boldsymbol{F}^{nc}(\psi)\cos(n\psi)d\psi \tag{28d}$$
$$\boldsymbol{H}_{is\boldsymbol{F}^{nc}} = \frac{1}{\pi}\int_0^{2\pi} \boldsymbol{F}^{nc}(\psi)\sin(n\psi)d\psi \tag{28dd-f}$$
$$\boldsymbol{H}_{0\boldsymbol{F}^{ns}} = \frac{1}{2\pi}\int_0^{2\pi} \boldsymbol{F}^{ns}(\psi)d\psi \tag{28e}$$
$$\boldsymbol{H}_{ic\boldsymbol{F}^{ns}} = \frac{1}{\pi}\int_0^{2\pi} \boldsymbol{F}^{ns}(\psi)\cos(n\psi)d\psi \tag{28f}$$
$$\boldsymbol{H}_{is\boldsymbol{F}^{ns}} = \frac{1}{\pi}\int_0^{2\pi} \boldsymbol{F}^{ns}(\psi)\sin(n\psi)d\psi \tag{28fg-i}$$

where:

$$\boldsymbol{F}^{nc}(\psi) = \boldsymbol{F}(\psi)\cos\psi \tag{29a}$$
$$\boldsymbol{F}^{ns}(\psi) = \boldsymbol{F}(\psi)\sin\psi \tag{29b}$$

Because the periodicity in Eq. (24) is limited to frequencies of one per forcing cycle, it is sufficient to retain up to the first harmonic in the harmonic decomposition of state vector in Eq. (25). By doing so, the LTP system in Eq. (24) is transformed into an equivalent LTI system with a system matrix:

$$\boldsymbol{A} = \begin{bmatrix} 0 & \frac{g}{L} & 0 & 0 & 0 & \Omega^2\frac{a}{2L} \\ 1 & 0 & 0 & 0 & 0 & 0 \\ 0 & 0 & 0 & \frac{g}{L} & -\Omega & 0 \\ 0 & 0 & 1 & 0 & 0 & -\Omega \\ 0 & \Omega^2\frac{a}{L} & \Omega & 0 & 0 & \frac{g}{L} \\ 0 & 0 & 0 & \Omega & 1 & 0 \end{bmatrix} \tag{30}$$

and where $\boldsymbol{x}^T = \left[\dot{\theta}_0\ \theta_0\ \dot{\theta}_{1c}\ \theta_{1c}\ \dot{\theta}_{1s}\ \theta_{1s}\right]$ is the augmented state vector. The stability of the system will be determined by the eigenvalues of the $\boldsymbol{A}$ matrix. The eigenvalues are given by:

$$\lambda_{1,2} = \pm c_1 \tag{31a}$$
$$\lambda_{3,4} = \pm c_2 \tag{31b}$$
$$\lambda_{5,6} = \pm\sqrt{c_3 + c_4 - \frac{c_5}{c_3}} \tag{31c}$$

where:

$$c_1 = \sqrt{c_4 - \frac{c_3}{2} + \frac{c_5}{2c_3} - \frac{1}{2}\sqrt{3}\left(c_3\frac{c_5}{c_3}i\right)} \tag{32a}$$
$$c_2 = \sqrt{c_4 - \frac{c_3}{2} + \frac{c_5}{2c_3} + \frac{1}{2}\sqrt{3}\left(c_3\frac{c_5}{c_3}i\right)} \tag{32b}$$
$$c_3 = \left\{c_6 + \sqrt{\left[c_6 + \frac{\left(6L^2g - 4L^3\Omega^2\right)^3}{216L^9} - c_7\right]^2 + c_5^3} + \frac{\left(6L^2g - 4L^3\Omega^2\right)^3}{216L^9} - c_7\right\}^{1/3} \tag{32c}$$
$$c_4 = \frac{6L^2g - 4L^3\Omega^2}{6L^3} \tag{32d}$$
$$c_5 = \frac{2L^3\Omega^4 - L\Omega^4a^2 + 6Lg^2}{6L^3} - \frac{\left(6L^2g - 4L^3\Omega^2\right)^2}{36L^6} \tag{32e}$$
$$c_6 = \frac{2L^2\Omega^4g - L\Omega^6a^2 + 4L\Omega^2g^2 - \Omega^4a^2g + 2g^3}{4L^3} \tag{32f}$$
$$c_7 = \frac{\left(6L^2g - 4L^3\Omega^2\right)\left(2L^3\Omega^4 - L\Omega^4a^2 + 6Lg^2\right)}{24L^6} \tag{32g}$$

It can be shown (Ref. 3) that the inverted pendulum is strongly stable (*i.e.*, stable for a high-enough forcing frequency) if:

$$a < \frac{\pi^2}{32}L \tag{33}$$

Consider an inverted pendulum where $g = 9.81$ m/s^2, $L = 1$ m, and $a = \frac{1}{2}\left(\frac{\pi^2}{32}L\right)$. Then, this pendulum will be stable for forcing frequencies $\Omega \gtrapprox 40.59$ rad/s. For instance, the eigenvalues for the case where $\Omega = 0$ rad/s (*i.e.*, no periodic forcing) are:

$$\lambda_1 = 3.1321, \quad \lambda_2 = -3.1321 \tag{34}$$

whereas the eigenvalues for the case where $\Omega = 50$ rad/s are:

$$\lambda_{1,2} = \pm 4.5314i, \quad \lambda_{3,4} = \pm 47.4166i, \quad \lambda_{5,6} = \pm 51.9779i \tag{35}$$

The order of the system in Eq. (26) can be reduced by means of residualization. As such, the augmented state vector is partitioned into fast and slow components, such that the slow states are chosen as the zeroth harmonic states, whereas the fast states are taken as the higher harmonics:

$$\boldsymbol{X}_{\mathrm{s}} = \boldsymbol{x}_0 \tag{36a}$$
$$\boldsymbol{X}_{\mathrm{f}}^T = \left[\boldsymbol{x}_{1c}^T\ \boldsymbol{x}_{1s}^T\right] \tag{36b}$$

Then, the submatrices of Eq. (12) become:

$$\boldsymbol{A}_{\mathrm{s}} = \begin{bmatrix} 0 & \frac{g}{L} \\ 1 & 0 \end{bmatrix} \tag{37a}$$

$$\boldsymbol{A}_{\mathrm{sf}} = \begin{bmatrix} 0 & 0 & 0 & \Omega^2 \frac{a}{2L} \\ 0 & 0 & 0 & 0 \end{bmatrix} \tag{37b}$$

$$\boldsymbol{A}_{\mathrm{f}} = \begin{bmatrix} 0 & \frac{g}{L} & -\Omega & 0 \\ 1 & 0 & 0 & -\Omega \\ \Omega & 0 & 0 & \frac{g}{L} \\ 0 & \Omega & 1 & 0 \end{bmatrix} \tag{37c}$$

$$\boldsymbol{A}_{\mathrm{fs}} = \begin{bmatrix} 0 & 0 \\ 0 & 0 \\ 0 & \Omega^2 \frac{a}{L} \\ 0 & 0 \end{bmatrix} \tag{37d}$$

Applying Eq. (14) yields the following residualized dynamics:

$$\hat{\boldsymbol{A}} = \begin{bmatrix} 0 & \frac{g}{L} - \frac{\Omega^4 a^2}{2L\left(L\Omega^2 + g\right)} \\ 1 & 0 \end{bmatrix} \tag{38}$$

The eigenvalues of this matrix are:

$$\lambda_{1,2} = \pm \frac{\sqrt{2}\sqrt{-\Omega^4 a^2 + 2L\Omega^2 g + 2g^2}}{2\sqrt{L}\sqrt{L\Omega^2 + g}} \tag{39}$$

Setting $\Re\left(\lambda_{1,2}\right) = 0$, solving for Ω, and discarding any non-physical solution yields:

$$\begin{aligned} \Omega &= \pm \frac{1}{a}\sqrt{Lg + \sqrt{L^2 g^2 + 2a^2 g^2 + a^2}} \\ &\approx 28.89 \text{ rad/s} \end{aligned} \tag{40}$$

Note that this is only an approximation to the minimum frequency that yields neutral stability.

SIMULATION MODELS

Helicopter Flight Dynamics Model

The nonlinear flight dynamics of a utility helicopter are modeled using PSUHeloSim (Ref. 46), a MATLAB® implementation of the General Helicopter (GenHel) flight dynamics simulation model (Ref. 47) with improved rotor, trimming, and linearization routines. PSUHeloSim is representative of a utility helicopter similar to a UH-60. The model contains a 6-degree-of-freedom rigid-body dynamic model of the fuselage, nonlinear aerodynamic lookup tables for the fuselage, rotor blades, and empennage, rigid flap and lead-lag rotor blade dynamics, a three-state Pitt-Peters inflow model (Ref. 48), and a Bailey tail rotor model (Ref. 49). The state vector is:

$$\begin{aligned} \boldsymbol{x}^T = \big[& u\ v\ w\ p\ q\ r\ \phi\ \theta\ \psi\ x\ y\ z\ \beta_0\ \beta_{0D}\ \beta_{1c}\ \beta_{1s}\ \dot{\beta}_0\ \dot{\beta}_{0D}\ \dot{\beta}_{1c}\ \dot{\beta}_{1s} \\ & \zeta_0\ \zeta_{0D}\ \zeta_{1c}\ \zeta_{1s}\ \dot{\zeta}_0\ \dot{\zeta}_{0D}\ \dot{\zeta}_{1c}\ \dot{\zeta}_{1s}\ \lambda_0\ \lambda_{1c}\ \lambda_{1s}\ \lambda_{0T} \big] \end{aligned} \tag{41}$$

where:

$u,\ v,\ w$ are the longitudinal, lateral, and vertical velocities in the body-fixed frame,

$p,\ q,\ r$ are the roll, pitch, and yaw rates,

$\phi,\ \theta,\ \psi$ are the Euler angles,

$x,\ y,\ z$ are the positions in the North-East-Down (NED) frame,

$\beta_0,,\ \beta_{0D},\ \beta_{1c},\ \beta_{1s}$ are the flapping angles in multi-blade coordinates,

$\zeta_0,\ \zeta_{0D},\ \zeta_{1c},\ \zeta_{1s}$ are the lead-lag angles in multi-blade coordinates,

$\lambda_0,\ \lambda_{1c},\ \lambda_{1s}$, are the main rotor induced inflow ratio harmonics, and

λ_{0T} is the tail rotor induced inflow ratio.

The control vector is:

$$\boldsymbol{u}^T = \left[\delta_{\mathrm{lat}}\ \delta_{\mathrm{lon}}\ \delta_{\mathrm{col}}\ \delta_{\mathrm{ped}}\right] \tag{42}$$

where δ_{lat} and δ_{lon} are the lateral and longitudinal cyclic inputs, δ_{col} is the collective input, and δ_{ped} is the pedal input.

External Slung Load

A non-linear model of dual-point suspend external slung load was developed in Ref. 10. This simulation was used to model a 6x6x8 ft, 2400 lbs, CONEX cargo container carried in an inverted V configuration as shown in Fig. 3. The hook geometry imitates a CH-47 Chinook with a spacing of 13.3 ft between the forward and rear cargo hooks. A conventional rigging procedure with four equal-length cables was applied with cable length equal to 16 ft. In the simulation, the dynamics of the CONEX container are isolated, *i.e.*, assumed to be not coupled to the rotorcraft flight dynamics, but subject to aerodynamic forces due to the forward flight condition of the rotorcraft. The simulation model includes non-linear look-up tables of aerodynamic coefficients based on static wind tunnel tests, a transfer function representing certain unsteady aerodynamic forces, a non-linear model of the forces due to cable stretching, and a complete non-linear 6-DOF dynamic model using representative mass and inertia properties of the load. The simulation model was partially validated against wind tunnel tests of a scale model in Ref. 10.

The dynamics of this load are known to exhibit unstable oscillations over certain airspeed ranges. The instability was observed in both simulation and wind tunnel tests in Ref. 10 and has been observed for similar dual-point suspended loads in flight tests. During instability events, the load will typically enter a prescribed periodic motion primarily involving roll and yaw oscillations but with some pitch motion as well. The trajectory is representative of a Limit Cycle Oscillation (LCO). The LCO orbits an unstable, static equilibrium point (a stationary point). If the load is trimmed at the static equilibrium, any small disturbance will cause the load to depart and enter the LCO orbit. The amplitude of the LCO is often large enough to be objectionable to the pilot or even present a hazard to the rotorcraft.

In Ref. 10, a load stablization controller was investigated using a laterally active forward cargo hook (ACH). The controller used feedback of cable angle and/or inertial measurements of the external load to drive the forward cargo hook

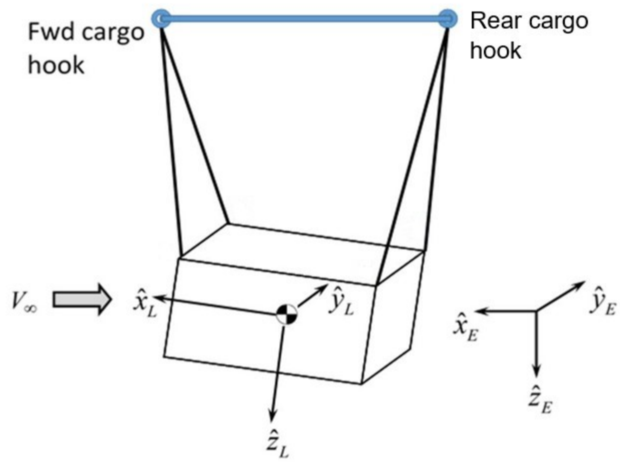

Fig. 3: Simulated slung load model expressed in load-fixed (L) and inertial (E) coordinate systems

lateral position in such a way that the load stabilizes at the static equilibrium point. The objective of this part of the study is to investigate the feasibility of stabilizing the load using an ACH oscillation of fixed frequency and amplitude without use of feedback, *i.e.*, use the ACH to provide vibrational stability of the load.

RESULTS

Vibrational Stabilization due to Blade Imbalance

Consider now an example involving the flight dynamics of a helicopter. Since helicopters are subjected to a variety of vibrations, it is feasible that vibrational effects might affect their stability characteristics. Traditionally, linear time invariant models of helicopter flight dynamics neglect vibrational effects, but through the use of harmonic decomposition (Ref. 28) time periodic terms can be retained in the LTI models.

In general, the flight dynamics of this model are non-linear time-periodic (NLTP), such that:

$$\dot{\boldsymbol{x}} = \boldsymbol{f}(\boldsymbol{x}, \boldsymbol{u}, \psi) \tag{43}$$

where $\psi = \Omega t$ is the azimuth angle of a reference main rotor blade. Blade imbalance is modeled by assuming one of the four rotor blades to have a different mass with respect to the others. Given this difference in mass, first and second flapping moments are varied accordingly. Because blade imbalance results in a periodic forcing at one-per-rotor-revolution (1/rev), trim at hover will no longer be represented a single point in the state space but rather by a periodic orbit such that the trim state and control vectors are $\boldsymbol{x}^*(\psi) = \boldsymbol{x}^*(\psi + \Omega T)$ and $\boldsymbol{u}^*(\psi) = \boldsymbol{u}^*(\psi + \Omega T)$.

To solve for this periodic orbit, the modified harmonic balance algorithm of Ref. 40 is used. Figure 4 shows the periodic trim acceleration at the center of gravity (CG) over one rotor revolution. In this figure, it is shown how rotor blade imbalance results in 1/rev vibrations with amplitudes of up to 0.5 g in the lateral and vertical acceleration for the 10% blade imbalance case. For reference, these vibrations are in line with those encountered by fixed-wing aircraft in severe turbulence (Refs. 50–53).

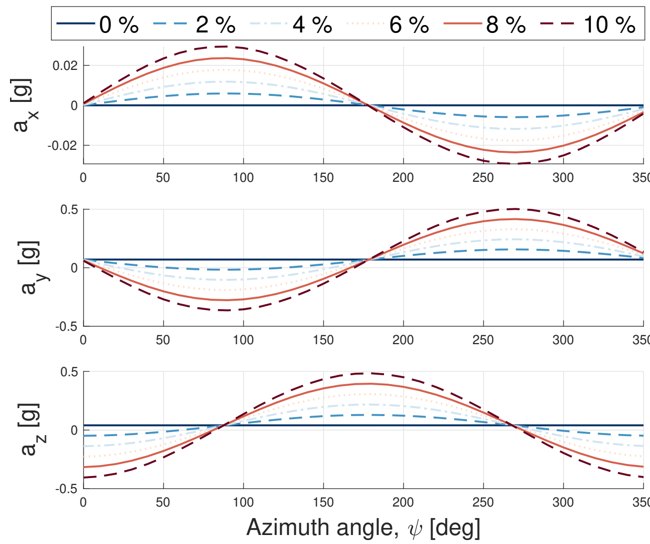

Fig. 4: Periodic trim acceleration at the CG over one rotor revolution for increasing blade imbalance.

Next, the flight dynamics are linearized about this periodic orbit to yield an LTP system. The LTP system is approximated with a higher-order LTI system by retaining up to the fourth harmonic of the fundamental frequency (*i.e.*, the angular speed of the main rotor Ω) in the states and output vectors (*i.e.*, $N = 4$ and $L = 4$), while retaining only the zeroth harmonic of the control input vector (*i.e.*, $M = 0$). While the dominant oscillations at hover will be the 1/rev oscillations due to blade imbalance, small 4/rev oscillations may also be present, although these become significant only in forward flight. Thus, the choice of retaining up to the fourth harmonic in the states and outputs. Retaining only the zeroth harmonic in the control input relies on the assumption that no higher-harmonic control (HHC) is employed, which is typically the case for conventional rotorcraft.

The order of the higher-order LTI model is subsequently reduced to a 10-state model representative of the rigid-body dynamics and of the regressive flap mode. An 8-state model is also obtained, which is representative of the rigid-body dynamics only. Because this model does not retain the flapping states used to predict the regressive flap mode, its accuracy will be limited to frequencies up to approximately 4 rad/s. To validate the linearized models obtained via the proposed method, the on-axis frequency responses of these models are compared to frequency responses extracted from frequency sweeps (Ref. 54). Because the dynamics of rotorcraft are unstable at hover, a control law similar to that in Ref. 46 was used to stabilize the hover dynamics during the frequency sweeps. Figure 5 shows the bare-airframe roll rate due to lateral input frequency responses for varying blade imbalance. Figure 5a corresponds to no blade imbalance, whereas 5b corresponds to a 10% blade imbalance. These figures show that the frequency responses of high-order LTI model match those obtained from frequency sweeps for both case, validating the LTI model. The 8-state model is shown to provide good accuracy up to about 4 rad/s, whereas the accuracy of the 10-state model extends up to about 10.5 rad/s. These results suggest that the linearization, harmonic decomposition, and successive model-order reduction are suitable for obtaining linearized models representative of rotor blade imbalance.

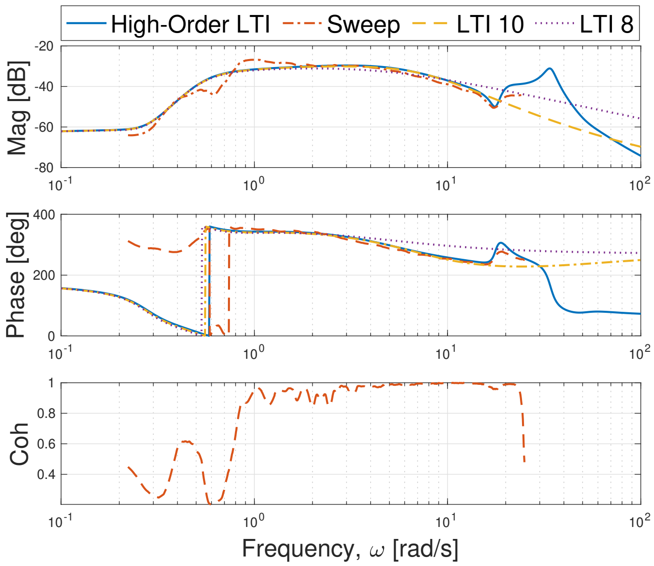

(a) 0% blade imbalance.

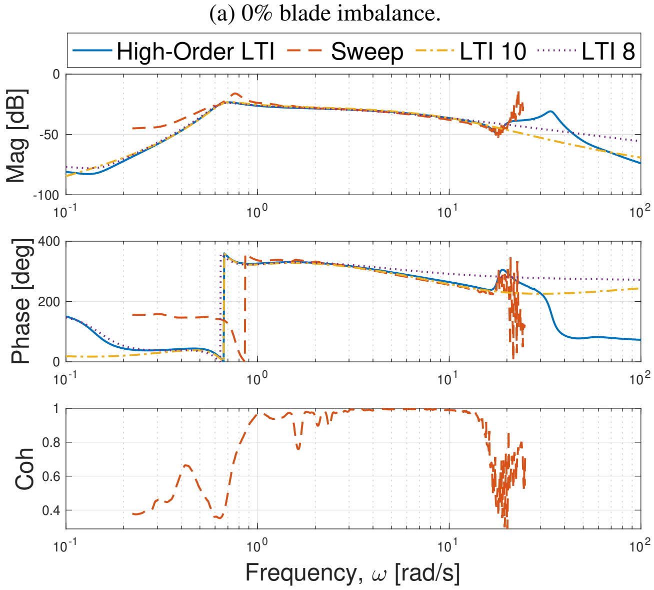

(b) 10% blade imbalance.

Fig. 5: Comparison between the roll rate due to lateral input frequency responses, $\frac{p}{\delta_{\text{lat}}}(s)$, obtained from linearized models and frequency sweeps.

The effect of blade imbalance on the flight dynamics can be assessed via spectral analysis of the reduced-order system thus obtained. Figure 6 shows the eigenvalues of the 10-state model for blade imbalance varying from zero to 10%. Figure 6a shows all ten eigenvalues and the regressive flapping eigenvalues are clearly shown to migrate to the left of the complex plane for increasing imbalance, eventually converging to fixed values. Figure 6b shows a detail of the rigid-body dynamics eigenvalues, where both the roll and pitch subsidence mode eigenvalues move toward the origin for increasing blade imbalance. This means that their frequency decreases with increasing blade imbalance. Moreover, both the roll and pitch oscillation eigenvalues move away from the origin along the imaginary axis, which is indicative of higher frequency and lower damping. One difference, though, is that the pitch oscillation eigenvalues move slightly to the right whereas the roll oscillatory eigenvalues move slightly to the left. The poles of the coupled yaw-heave mode are relatively unaffected compared to the other modes. These results are reported quantitatively in Table 1 for two cases: zero blade imbalance and 10% blade imbalance. Thus, it is concluded that rotor blade imbalance has a symmetric effect on roll and pitch axes, in that it tends to decrease the frequency of the subsidence modes of the hovering cubic (Ref. 4), while the oscillatory modes tend to increase in frequency and decrease in damping.

Figure 7 shows the lateral (Fig. 7a) and longitudinal (Fig. 7b) stability derivatives of the 8-state model for varying blade imbalance. The magnitude of the roll and pitch axes damping derivatives L_p and M_q is shown to decrease with increasing blade imbalance. On the other hand, while lateral speed stability (Y_b) becomes more negative with increasing blade imbalance, longitudinal speed stability (X_u) decreases in magnitude. The roll and pitch moment derivatives due to lateral and logitudinal speed, respectively, show similar trennds in that both become more negative. These results indicate that, indeed, rotor blade imbalance affects the eigenvalues of a rotorcraft at hover.

In light of these results, the dynamics identified for a helicopter with an imbalanced rotor may indeed differ from those obtained from simulations where the rotor is perfectly balanced. A more in-depth explanation follows. When performing system/parametric identification from flight test data, which inevitably corresponds to some rotor imbalance on the real aircraft, what is identified are, in fact, dynamics equivalent to the residualized dynamics from the high-order LTI model. These can be referred to as the "true" dynamics. On the other hand, when performing flight dynamics predictions from physics-based simulations, any periodic component in the flight dynamics due to blade imbalance is not modeled in that rotor blades are typically assumed as perfectly balanced. Even if blade imbalance was modeled, flight dynamics predictions adopting linearized models only typically consider the averaged (or zeroth harmonic) dynamics. This is equivalent to performing eigenanalysis on the averaged portion of the high-order LTI system in harmonic decomposition form. Or, in other terms, it corresponds to performing eigenanalysis on a reduced-order system obtained by truncating all of the higher-harmonic states from the high-order LTI system. Thus, any harmonic component is ignored. It is worth noting that the averaged dynamics of all cases presented with rotor imbalance is in fact the same. This concept is illustrated in Fig. 8, which features the frequency response of the ze-

Table 1: Hover modal characteristics for varying blade imbalance.

Mode	Imbalance [%]	Eigenvalues [rad/s]	Natural Frequency, ω_n [rad/s]	Damping Ratio, ζ
Roll Subsidence	0	-5.5645	-	1
	10	-3.9270	-	1
Pitch Subsidence	0	-1.7763	-	1
	10	-1.5681	-	1
Roll Oscillation	0	$0.4980 \pm 0.4364i$	0.6622	-
	10	$0.4624 \pm 0.6305i$	0.7819	-
Pitch Oscillation	0	$-0.2348 \pm 0.4856i$	0.5394	0.4353
	10	$-0.1106 \pm 0.6601i$	0.6693	0.1730
Coupled Yaw-Heave	0	$-0.2924 \pm 0.0470i$	0.2962	0.9873
	10	$-0.1106 \pm 0.6601i$	0.2994	0.9799

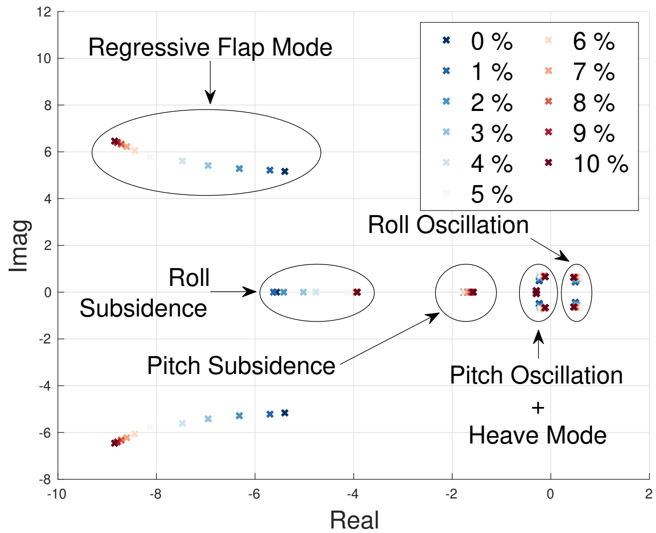

(a) Rigid-body and regressive flap dynamics.

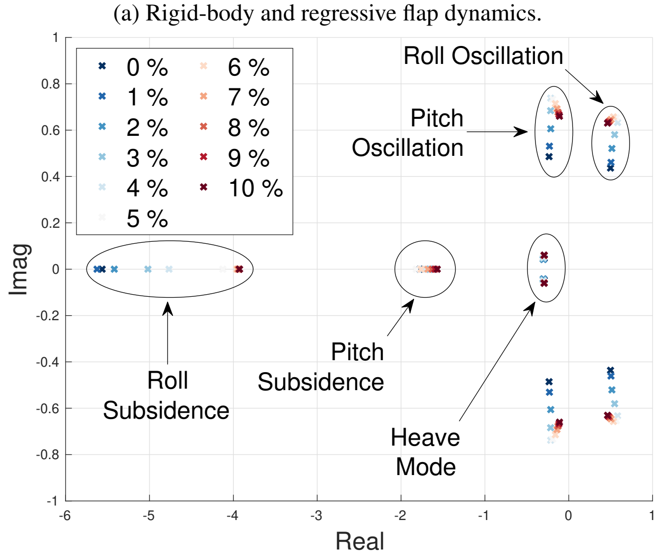

(b) Rigid-body dynamics.

Fig. 6: Hover eigenvalues of the 10-state residualized model for varying blade imbalance.

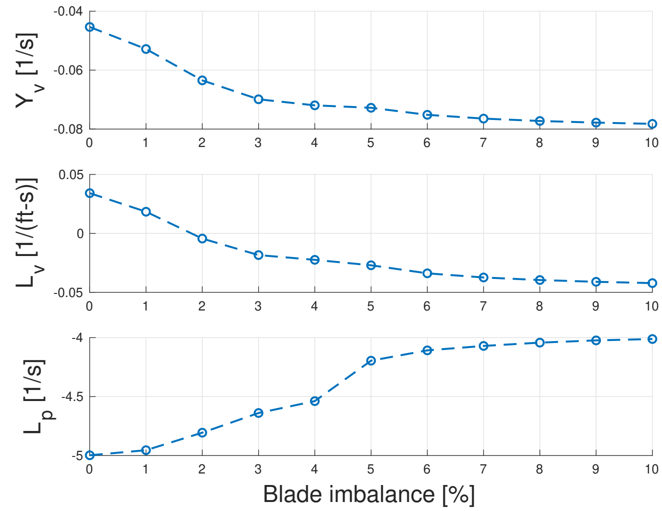

(a) Lateral stability derivatives.

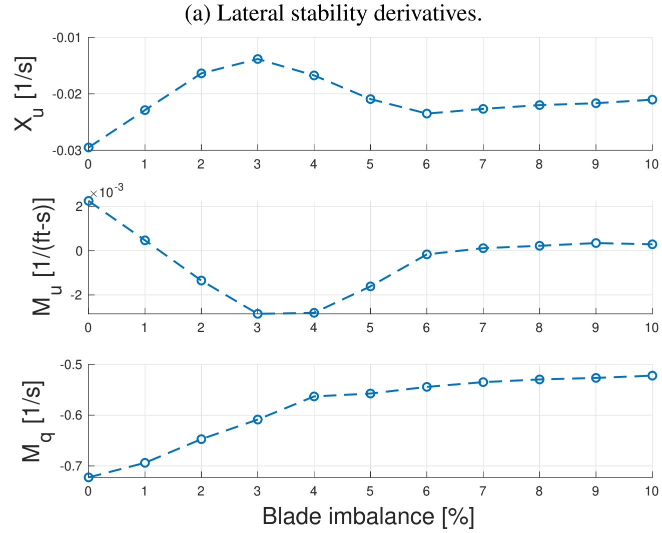

(b) Longitudinal stability derivatives.

Fig. 7: Hover stability derivatives for varying blade imbalance.

roth harmonic of the roll rate to lateral inputs, *i.e.*, $\frac{p_0}{\delta_{\text{lat}}}(s)$, for the high-order LTI model in harmonic decomposition form representative of a 10% rotor blade imbalance, the averaged dynamics, and the 8- and 10-state residualized models corresponding to a 10% rotor blade imbalance. The 8-state residualized model constitutes a good approximation of the high-order LTI up to approximately 4 rad/s. In fact, the 8-state model shows reduced phase roll-off after 4 rad/s. This is because it does not include the longitudinal and lateral flapping states needed to predict the regressive flap mode. The 10-state model is accurate up to approximately 10.5 rad/s. The average dynamics, however, fails to predict the response in low-to-mid frequencies of interest to flight dynamics (*i.e.*, 0.3 to 30 rad/s). These differences will cause discrepancies in the estimation of the stability derivative L_p. The same concept applies to all other frequency responses of interest for the identification of reduced-order models of the rotorcraft flight dynamics.

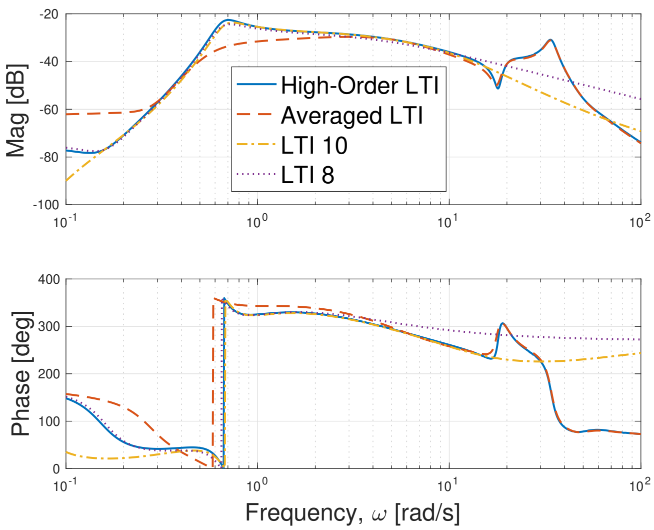

Fig. 8: Frequency response of the zeroth harmonic of the roll rate to lateral inputs, $\frac{p_0}{\delta_{\text{lat}}}(s)$.

Vibrational Stabilization of an External Slung Load

This analysis focused on the dual-point external load dynamics at 78 knots forward airspeed. In this flight condition, the external load exhibits a lateral-directional LCO as illustrated in Fig. 9. In this simulation the external load starts in a static equilibrium with a slight pitch attitude due to the drag forces on the load. A ± 0.1 ft perturbation is applied to the forward cargo hook at 10 seconds, which initiates a divergence (since the static equilibrium is unstable) until the load reaches a stable LCO with an amplitude of about ± 12 deg in yaw and ± 8 deg in roll. The roll-yaw trajectory of the LCO, shown in Fig. 10, is not a simple elliptical orbit but a fairly complex trajectory due to the non-linear load dynamics.

Through trial-and-error it was found that with small amplitude excitation of the ACH at 7 rad/sec, the simulated load stayed closer to the static equilibrium point and remained in a small amplitude orbit (much smaller amplitude oscillations than the LCO shown in Fig. 10). The time history response is shown in Fig. 11, where a ± 0.04 ft (1.2 cm), 7 rad/sec sine wave is applied to the forward cargo hook. At 10 seconds, the same perturbation ± 0.1 ft perturbation used in Fig. 9 is super-imposed on the cargo hook. The response shows that the response of the external load remains very small, less than 0.3 deg roll and yaw oscillations. The roll-yaw trajectory is shown in Fig. 12. If there is no perturbation applied to the system, a small amplitude roll-yaw oscillation is observed in red. This oscillation scales with the amplitude of the ACH input down to a certain limit (for amplitudes much lower than ± 0.04 ft the load will depart to the large amplitude LCO). Following the perturbation we see the load response remains small over a long period of time, but there is a lower frequency oscillation superimposed on the roll response. Nonetheless, the simulations indicate the forced response is at least marginally stable and the small oscillation of the ACH prevents the load from entering the large amplitude LCO.

It should be noted that there were some discrepancies between the wind tunnel tests and simulation model presented in Ref. 10, but the qualitative behavior was similar between test and simulation. The wind tunnel tests showed a somewhat higher amplitude LCO at an airspeed of 78 knots full-scale (12 m/s model-scale), with $+15/-20$ deg oscillations in yaw and $+10/-8$ oscillation in roll, but with similar trajectory shape. Frequency sweeps were performed on the ACH at 78 knots full-scale airspeed, and significant reductions in load oscillations were observed around 4.1 rad/sec ACH inputs, possibly indicating vibrational stability at a somewhat lower driving frequency.

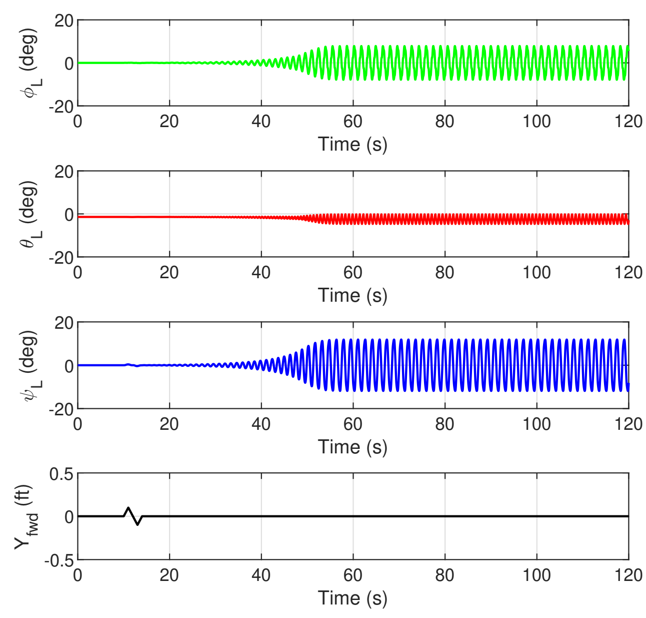

Fig. 9: Time history of external load LCO at 78 knots forward airspeed.

CONCLUSIONS

This paper investigated vibrational stabilization effects in rotorcraft flight dynamics. Starting from a simple example involving an inverted pendulum, the use of the harmonic decomposition method for the study of vibrational stabilization effects was demonstrated. The concept was then extended to

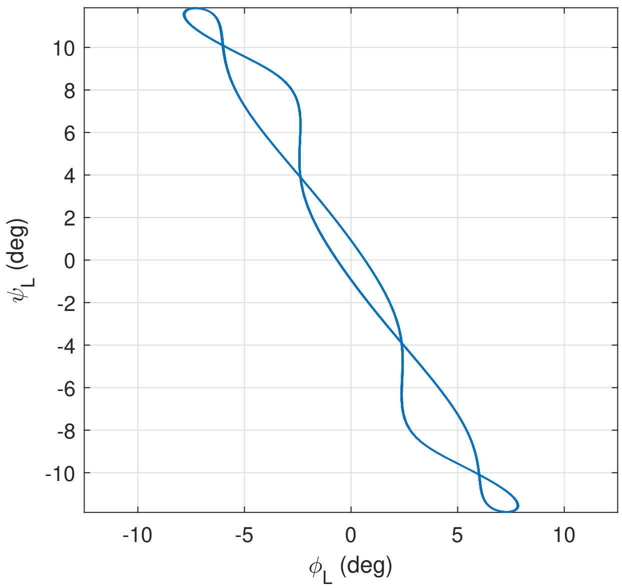

Fig. 10: External load LCO trajectory at 78 knots forward airspeed.

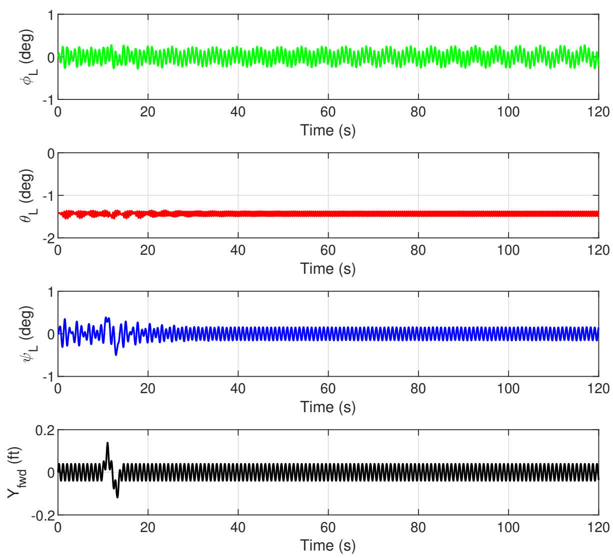

Fig. 11: Time history of external load at 78 knots dorward airspeed with vibrational stability.

analyze the effect of blade imbalance on the flight dynamics of a helicopter, as well as vibrational stablization of a slung load in forward flight using small-amplitude and disturbances on an active cargo hook. Based on this work, the following conclusions can be reached:

1. While vibrations induced by rotor blade imbalance did not stabilize the hovering dynamics of a helicopter, these vibrations still have a significant effect on the hovering dynamics. Increasing rotor blade imbalance results in a symmetric effect on the roll and pitch axes, in that it tends to decrease the frequency of the subsidence modes of the hovering cubic, while the unstable oscillatory modes tend to increase in frequency and decrease in damping. To the contrary, the yaw/heave dynamics are

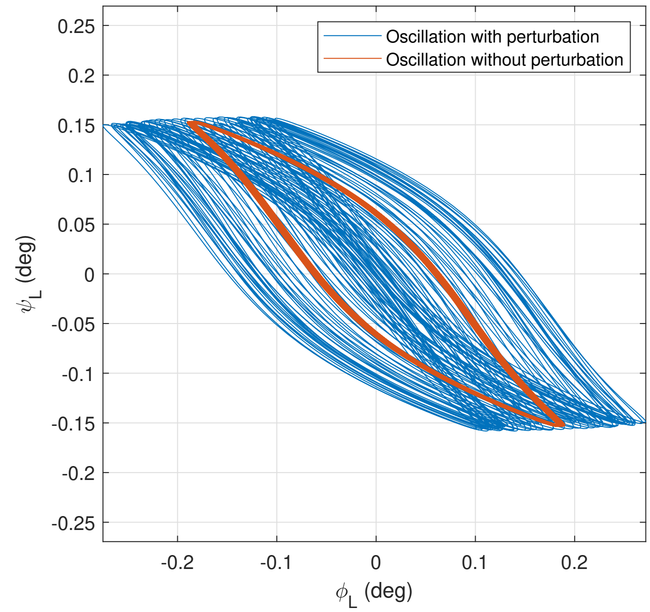

Fig. 12: External load trajectory at 78 knots forward airspeed with vibrational stability.

relatively unaffected compared to the lateral and longitudinal axes.

2. Commonly observed mismatches between the flight identified dynamics and those predicted via physics-based models may indeed be ascribed vibrational stability effects due to rotor blade imbalance. This is because when performing system/parametric identification from flight test data, which inevitably corresponds to some rotor imbalance on the real aircraft, what is identified are, effectively, dynamics equivalent to the residualized dynamics obtained from the linearized time-periodic dynamics. On the other hand, when performing flight dynamics predictions from physics-based simulations, any periodic component in the flight dynamics due to blade imbalance is not modeled in that rotor blades are typically assumed as perfectly balanced. Moreover, typical flight dynamics predictions only adopt the averaged linearized dynamics. As such, any time-periodic effect that may have an effect on the flight dynamics is typically ignored in analyses from simulations while periodicity will show up in models identified from flight test data.

3. A small-amplitude oscillation of the active cargo hook (ACH) at 7 rad/s resulted in the simulated load to stay closer to the static equilibrium point and to remain in an orbit significantly smaller (less than 0.3 deg roll and yaw oscillations) than the limit cycle it incurred in with no ACH periodic forcing ($\pm$12 deg in yaw and $\pm$8 deg in roll oscillations). The simulated load oscillation amplitude scales with the amplitude of the ACH input down to a certain limit.

4. Simulations indicate the forced response is stable and the small oscillation of the ACH prevents the load from entering the high amplitude LCO. These results are in line

with previous research showing that slung loads can exhibit better stability /lower amplitude oscillations when subjected to periodic disturbances at the hook. This potentially constitutes a practical solution to the semi-active control of a suspended load.

REFERENCES

[1]Meerkov, S., “Principle of vibrational control: Theory and applications,” *IEEE Transactions on Automatic Control*, Vol. 25, (4), 1980, pp. 755–762.
doi: https://doi.org/10.1109/TAC.1980.1102426

[2]Bellman, R., Bentsman, J., and Meerkov, S., “Vibrational control of nonlinear systems: Vibrational stabilizability,” *IEEE Transactions on Automatic Control*, Vol. 31, (8), 1986, pp. 710–716.
doi: https://doi.org/10.1109/TAC.1986.1104384

[3]Levi, M. and Weckesser, W., “Stabilization of the Inverted Linearized Pendulum by High Frequency Vibrations,” *SIAM Review*, Vol. 37, (2), 1995, pp. 219–223.
doi: https://doi.org/10.1137/1037044

[4]McRuer, D. T., Ashkenas, I. L., and Graham, D., *Aircraft Dynamics and Automatic Control*, Princeton University Press, Princeton, NJ, 1973, Chapter 6.

[5]Taha, H. E., Tahmasian, S., Woosley, C. A., Nafayeh, A. H., and Hajj, M. R., “The Need for Higher-Order Averaging in the Stability Analysis of Hovering, Flapping-Wing Flight,” *Bioinspiration & Biomimetics*, Vol. 10, (1), 2015, pp. 1–15.
doi: https://doi.org/10.1088/1748-3190/10/1/016002

[6]Taha, H. E., Kiani, M., Hendrick, T. L., and Greeter, J. S. M., “Vibrational control: A hidden stabilization mechanism in insect flight,” *Science Robotics*, Vol. 5, (46), 2020.
doi: https://doi.org/10.1126/scirobotics.abb1502

[7]Saetti, U., Horn, J. F., Berger, T., Lopez, M. J. S., and Tischler, M. B., “Identification of Linear Time-Periodic Systems from Rotorcraft Flight Test Data,” *Journal of Guidance, Control, and Dynamics*, Vol. 42, (10), 2019, pp. 2288–2296.
doi: https://doi.org/10.2514/1.G004406

[8]Hayajnh, M. A., Saetti, U., and Pradad, J. V. R., “Identification of High-Order Linear Time-Invariant Models From Periodic Nonlinear System Responses,” Proceedings of the VFS Aeromechanics for Advanced Vertical Flight Technical Meeting, San Jose, CA, Jan 25-27, 2022.

[9]Saetti, U. and Rogers, J. D., “Harmonic Decomposition Models of Flapping-Wing Flight for Stability Analysis and Control Design,” *Journal of Guidance, Control, and Dynamics*, Vol. 45, (8), Aug 2022.
doi: https://doi.org/10.2514/1.G006447

[10]Chen, Z., Horn, J., Enciu, J., Raz, R., Rosen, A., and Cicolani, L., “Examination of Dynamic Characteristics of a CONEX Container in Dual Point Carriage from Simulation and Wind Tunnel Test,” Proceedings of the 49th European Rotorcraft Forum, Bückeburg, Germany, September 5–7, 2023.

[11]Maggia, M., Eisa, S. A., and Taha, H. E., “On higher-order averaging of time-periodic systems: reconciliation of two averaging techniques,” *Nonlinear Dynamics*, Vol. 99, 2020, pp. 813–836.
doi: https://doi.org/10.1007/s11071-019-05085-4

[12]Floquet, G., “Sur les équations différentielles linéaires à coefficients périodiques,” *Annales scientifiques de l’École Normale Supérieure*, Vol. 2, (12), 1883, pp. 47–88.
doi: https://doi.org/10.24033/asens.220

[13]Dietl, J. M. and Garcia, E., “Stability in Ornithopter LongitudinalFlight Dynamics,” *Journal of Guidance, Control, and Dynamics*, Vol. 31, (4), 2008, pp. 1157–1152.
doi: https://doi.org/10.2514/1.33561

[14]Bierling, T. and Patil, M., “Stability and Power Optimality in Time-Periodic Flapping Wing Structures,” *Journal of Fluids and Structures*, Vol. 38, 2013, pp. 238–254.
doi: https://doi.org/10.1016/j.jfluidstructs.2012.12.006

[15]Su, W. and Cesnik, C. E. S., “Flight Dynamic Stability of a Flapping Wing Micro Air Vehicle in Hover,” Proceedings of the 52nd AIAA/ASME/ASCE/AHS/ACS Structures, Structural Dynamics, and Materials Conference, Denver, CO, April 4-7, 2011.
doi: https://doi.org/10.2514/6.2011-2009

[16]Bolender, M. A., “Open-Loop Stability of Flapping Flight in Hover,” AIAA 2010-7552, AIAA Guidance, Navigation, and Control Conference, Toronto, Ontario, Canada, Aug 2-5, 2010.
doi: https://doi.org/10.2514/6.2010-7552

[17]Sanders, V. F., J. A. and Murdock, J., *Averaging Methods in Nonlinear Dynamical Systems*, Springer, Princeton, NJ, 2007, Chapter Averaging: the periodic case.
doi: https://doi.org/10.1007/978-0-387-48918-6

[18]Hassan, A. M. and Taha, H. E., “Higher-Order Averaging Analysis of the Nonlinear Time-Periodic Dynamics of Hovering Insects/Flapping-Wing Micro-Air-Vehicles,” Proceedings of the 55th Conference on Decision and Control, December 12-14, 2016.
doi: https://doi.org/10.1109/CDC.2016.7799424

[19]Oppenheimer, M. W., Weintraub, I. E., Sighorsson, and Doman, D. B., “Quarter Cycle Modulation of a Minimally Actuated Biomimetic Vehicle,” AIAA 2014-1467, AIAA SciTech Forum, National Harbor, MD, Jan 13-17, 2014.
doi: https://doi.org/10.2514/1.G000548

[20]Oppenheimer, M. W., Weintraub, I. E., Sighorsson, and Doman, D. B., “Control of a Minimally Actuated Biometric Vehicle Using Quarter-Cycle Wingbeat Modulation,” *Journal of Guidance, Control, and Dynamics*, Vol. 38, (7), 2015, pp. 1187–1196.
doi: https://doi.org/10.2514/1.G000548

[21]Sigthorsson, D. O., Oppenheimer, M. W., and Doman, D. B., "Flapping-Wing Micro-Air-Vehicle Control Employing Triangular Waves Strokes and Cycle Averaging," AIAA 2010-7553, AIAA Guidance, Navigation, and Control Conference, Toronto, Ontario, Canada, Aug 2-5, 2010.
doi: https://doi.org/10.2514/6.2010-7553

[22]Sigthorsson, D. O., Oppenheimer, M. W., and Doman, D. B., "Flapping-Wing Micro-Air-Vehicle 4-DOF Controller Applied to a 6-DOF Model," AIAA 2010-7554, AIAA Guidance, Navigation, and Control Conference, Toronto, Ontario, Canada, Aug 2-5, 2010.
doi: https://doi.org/10.2514/6.2010-7554

[23]Finio, B. M., Perez-Arancibia, N. O., and Wood, R. J., "System Identification and Linear Time-Invariant Modeling of an Insect-Sized Flapping-Wing Micro Air Vehicle," 2011 IEEE/ESJ International Conference on Intelligent Robots and Systems, San Francisco, CA, Sep 25-30, 2011.
doi: https://doi.org/10.1109/IROS.2011.6094421

[24]Cheng, D. and Deng, X., "Translational and Rotational Damping of Flapping Flight and Its Dynamics and Stability at Hovering," *IEEE Transactions on Robotics*, Vol. 27, (5), 2011, pp. 849 – 864.
doi: 10.1109/TRO.2011.2156170

[25]Vela, P. A., *Averaging and control of nonlinear systems (with application to biomimetic locomotion)*, Ph.D. thesis, California Institute of Technology, Pasadena, CA, May, 2003.

[26]Pandyan, R. and Sinha, S. C., "Time-Varying Controller Synthesis for Nonlinear Systems subjected to Periodic Parametric Loading," *Journal of Vibration and Control*, Vol. 7, (1), 2001, pp. 73–90.
doi: https://doi.org/10.1177/107754630100700105

[27]Colaneri, P., Celi, R., and Bittanti, S., "Constant Coefficient Representation of Discrete Periodic Linear Systems," Proceedings of the 4th Decennial Specialists' Conference on Aeromechanics, January 21-24, 2004.

[28]Lopez, M. J. S. and Prasad, J. V. R., "Linear Time Invariant Approximations of Linear Time Periodic Systems," *Journal of the American Helicopter Society*, Vol. 62, (1), jan 2017, pp. 1–10.
doi: 10.4050/jahs.62.012006

[29]Lopez, M. J. S., *LINEAR TIME INVARIANT APPROXIMATIONS OF LINEAR TIME PERIODIC SYSTEMS FOR INTEGRATED FLIGHT AND VIBRATION CONTROL*, Ph.D. thesis, Georgia Institute of Technology, Atlanta, GA, May, 2016.

[30]Saetti, U. and Horn, J. F., "Linear Time-Invariant Approximations of Nonlinear Time-Periodic Systems," *Journal of the American Helicopter Society*, Vol. 68, (1), jan 2023, pp. 1–10.
doi: https://doi.org/10.4050/JAHS.68.012006

[31]Prasad, J. V. R., Olcer, F. E., Sankar, L. N., and He, C., "Linear Time Invariant Models for Integrated Flight and Rotor Control," Proceedings of the 35th European Rotorcraft Forum, September 22-25, 2009.

[32]Lopez, M., Prasad, J. V. R., Tischler, M. B., Takahashi, M. D., and Cheung, K. K., "Simulating HHC/AFCS Interaction and Optimized Controllers using Piloted Maneuvers," Proceedings of the 71st Annual Forum of the American Helicopter Society, May 5-7, 2015.

[33]Padthe, A. K., Friedmann, P. P., Lopez, M., and Prasad, J. V. R., "Analysis of High Fidelity Reduced-Order Linearized Time-Invariant Helicopter Models for Integrated Flight and On-Blade Control Applications," Proceedings of the 41st European Rotorcraft Forum, Sep 1-4, 2015.

[34]Saetti, U. and Horn, J. F., "Load Alleviation Flight Control Design using High-Order Dynamic Models," *Journal of the American Helicopter Society*, Vol. 65, (3), 2020.
doi: https://doi.org/10.4050/JAHS.65.032009

[35]Saetti, U., Horn, J. F., Berger, T., and Tischler, M. B., "Handling-Qualities Perspective on Rotorcraft Load Alleviation Control," *Journal of Guidance, Control, and Dynamics*, 2020, pp. 1–13.
doi: https://doi.org/10.2514/1.G004965

[36]Scaramal, M., Horn, J. F., and Saetti, U., "Load Alleviation Control using Dynamic inversion with Direct Load Feedback," Proceedings of the 77th Annual Forum of the Vertical Flight Society, Virtual, May 10-14, 2021.

[37]Mballo, C. E. and Prasad, J. V. R., "A Real Time Scheme for Rotating System Component Load Estimation Using Fixed System Measurements," Proceedings of the 74th Annual Forum of the Vertical Flight Society, Phoenix, AZ, May 14-17, 2018.

[38]Mballo, C. E. and Prasad, J. V. R., "Real Time Rotor Component Load Limiting via Model Predictive Control," Proceedings of the 75th Annual Forum of the Vertical Flight Society, Philadelphia, PA, May 13-16, 2019.

[39]Saetti, U. and Lovera, M., "Time-Periodic and High-Order Time-Invariant Linearized Models of Rotorcraft: A Survey," *Journal of the American Helicopter Society*, Vol. 67, (1), 2022.
doi: https://doi.org/10.4050/JAHS.67.012008

[40]Saetti, U. and Rogers, J. D., "Revisited Harmonic Balance Trim Solution Method for Periodically-Forced Flight Vehicles," *Journal of Guidance, Control, and Dynamics*, Vol. 44, (5), May 2021, pp. 1008–1017.
doi: https://doi.org/10.2514/1.G005553

[41]Kokotovic, P. V., O'Malley, R. E., and Sannuti, P., "Singular Perturbations and Order Reduction in Control Theory, an Overview," *Automatica*, Vol. 12, (2), 1976, pp. 123–132.
doi: https://doi.org/10.1016/0005-1098(76)90076-5

[42]Frazzoli, E., Dahlel, M. A., and Feron, E., “Maneuver-Based Motion Planning for Nonlinear Systems With Symmetries,” *IEEE Transactions on Robotics*, Vol. 21, (6), Dec 2005, pp. 1077–1091.
doi: https://doi.org/10.1109/TRO.2005.852260

[43]Saetti, U. and Horn, J. F., “Load Alleviation Control Design Using Harmonic Decomposition Models, Rotor State Feedback, and Redundant Control Effectors,” American Helicopter Society 74th Annual Forum Proceedings, May 14-17, 2018.

[44]Saetti, U., *Rotorcraft Flight Control Design with Alleviation of Unsteady Rotor Loads*, Ph.D. thesis, Pennsylvania State University, University Park, PA, August, 2019.

[45]Berg, M. J. and Wickramasinghe, I. P. M., “Vibrational Control Without Averaging,” *Automatica*, Vol. 58, 2015, pp. 72–81.
doi: https://doi.org/10.1016/j.automatica.2015.04.028

[46]Horn, J. F., “Non-Linear Dynamic Inversion Control Design for Rotorcraft,” *Aerospace*, Vol. 6, (38), 2019.
doi: https://doi.org/10.3390/aerospace6030038

[47]Howlett, J. J., “UH-60A Black Hawk Engineering Simulation Program. Volume 1: Mathematical Model,” Technical report, NASA-CR-166309, 1980.

[48]Pitt, D. M. and Peters, D. A., “Theoretical Prediction of Dynamic-Inflow Derivatives,” Proceedings of the 6th European Rotorcraft and Powered Lift Aircraft Forum, September 16-19, 1980.

[49]Bailey, F. J., “A Simplified Theoretical Model of Determining the Characteristics of a Lifting Rotor in Forward Flight,” Technical report, NACA Report No. 716, 1941.

[50]Chan, S. T. and Mok, C. W., “Comparison of Doppler LIDAR Observations of Severe Turbulence and Aircraft Data,” American Metereological Society 11th Conference on Aviation, Range, and Aerospace Metereology, October 4-7, 2014.

[51]Koch, S. E., Jamison, B. D., Lu, C., Smith, T. L., Tollerud, E. I., Girz, C., Wang, N., Lane, T. P., Shapiro, M. A., Parrish, D. D., and Cooper, O. R., “Turbulence and Gravity Waves within an Upper-Level Front,” *Journal of the Atmospheric Sciences*, Vol. 62, (11), 2005, pp. 3885—-3908.
doi: https://doi.org/10.1175/JAS3574.1

[52]Crouse, G. L., “Design for Passenger Comfort and All Weather Operation,” 7th AIAA ATIO Conference, 2nd CEIAT International Conference on Innovation and Integration in Aero Sciences, 17th LTA Systems Technology Conference; followed by 2nd TEOS Forum, September 18-20, 2014.
doi: https://doi.org/10.2514/6.2007-7861

[53]Lee, D. B. and Chun, H. Y., “A Numerical Study of Aviation Turbulence Encountered on 13 February 2013 over the Yellow Sea between China and Korea,” *Journal of Applied Meteorology and Climatology*, Vol. 57, (4), 2018, pp. 1043—-1060.
doi: https://doi.org/10.1175/JAMC-D-17-0247.1

[54]Tischler, M. B. and Remple, R. K., *Aircraft and Rotorcraft System Identification, Second Edition*, American Institute of Aeronautics and Astronautics, second edition, 2012, Chapter 5, 13, 17.
doi: 10.2514/4.868207